

COSMOLOGICAL CONSTRAINTS FROM THE REDSHIFT DEPENDENCE OF THE GALAXY ANGULAR 2-POINT CORRELATION FUNCTION

XIAO-DONG LI,

School of Physics, Korea Institute for Advanced Study, 85 Heogiro, Dongdaemun-gu, Seoul 130-722, Korea

CHENG CHENG,

Kavli Institute for Theoretical Physics China, Institute of Theoretical Physics, Chinese Academy of Sciences, Zhong Guan Cun Street 55#, Beijing, 100190, P.R. China and
 University of Chinese Academy of Sciences, P.R. China

CHANGBOM PARK,

School of Physics, Korea Institute for Advanced Study, 85 Heogiro, Dongdaemun-gu, Seoul 130-722, Korea

CRISTIANO G. SABIU, HYUNBAE PARK,

Korea Astronomy and Space Science Institute, Daejeon 305-348, Korea

JUHAN KIM¹,

Center for Advanced Computation, Korea Institute for Advanced Study, 85 Hoegi-ro, Dongdaemun-gu, Seoul 130-722, Korea and
 School of Physics, Korea Institute for Advanced Study, 85 Heogiro, Dongdaemun-gu, Seoul 130-722, Korea

AND

SUNGWOOK E. HONG

School of Physics, Korea Institute for Advanced Study, 85 Heogiro, Dongdaemun-gu, Seoul 130-722, Korea

Draft version August 30, 2016

ABSTRACT

We use the shape of galaxy 2-point correlation function to measure the redshift dependence cosmology volume effect. ...

Keywords: large-scale structure of Universe — dark energy — cosmological parameters

1. INTRODUCTION

Dark energy ... Large scale structure...

2pCF is a good statistic... blahblah In 2d xi(s,mu)
 ... In *** we used the redshift dependence of 2pCF to probe the volume and AP effect... The method is applied to BOSS data in *** and obtain tight constraint...

In *** we further propose to use the shape of xi(s) to probe the volume effect... Stretch or compression shifts the clustering properties in some particular scale to larger or smaller scales... The shape of measured xi(s) is thus stretched or compressed.

The outline of this paper is as follows.

This paper is organized as follows... The outline of this paper proceeds as follows. In §2 we briefly review the nature and consequences of the AP effect and volume changes when performing coordinate transforms in a cosmological context. In §3 we describe the N-body simulations and mock galaxy catalogues that are used to test our methodology. In §4, we describe our new analysis method for quantifying the redshift dependence of volume effect. We conclude in §5.

2. GEOMETRIC DEFORMATION WHEN

In this section we briefly introduce the scaling effect in wrongly assumed cosmologies. A more detailed description has been provided in Li et al. (2014, 2015, 2016).

Suppose that we are probing the shape of some objects in the Universe. We measure its redshift span Δz and

angular size $\Delta\theta$, then compute its sizes in the radial and transverse directions from the relations of

$$\Delta r_{\parallel} = \frac{c}{H(z)} \Delta z, \quad \Delta r_{\perp} = (1+z) D_A(z) \Delta\theta, \quad (1)$$

where H is the Hubble parameter, D_A is the angular diameter distance. In the particular case of a flat universe with constant dark energy EoS, they take the forms of

$$H(z) = H_0 \sqrt{\Omega_m a^{-3} + (1 - \Omega_m) a^{-3(1+w)}}, \\ D_A(z) = \frac{1}{1+z} r(z) = \frac{1}{1+z} \int_0^z \frac{dz'}{H(z')}, \quad (2)$$

where $a = 1/(1+z)$ is the cosmic scale factor, H_0 is the present value of Hubble parameter and $r(z)$ is the comoving distance.

In case we adopted a wrong set of cosmological parameters in Equation (1,2), the inferred Δr_{\parallel} and Δr_{\perp} are wrong, resulting in distorted shape (AP effect) and wrongly estimated volume (volume effect). These effects have been discussed in Li et al. (2014, 2015, 2016). This paper we focus on the misestimation of Δr_{\perp} , which can be described by the following quantities

$$\alpha_{\perp} \equiv \frac{\Delta r_{\perp,\text{wrong}}}{\Delta r_{\perp,\text{true}}} = \frac{D_{A,\text{wrong}}}{D_{A,\text{true}}}, \quad (3)$$

where “true” and “wrong” denote the values of D_A in the true cosmology and wrongly assumed cosmology.

¹ Corresponding Author: kjhan@kias.re.kr

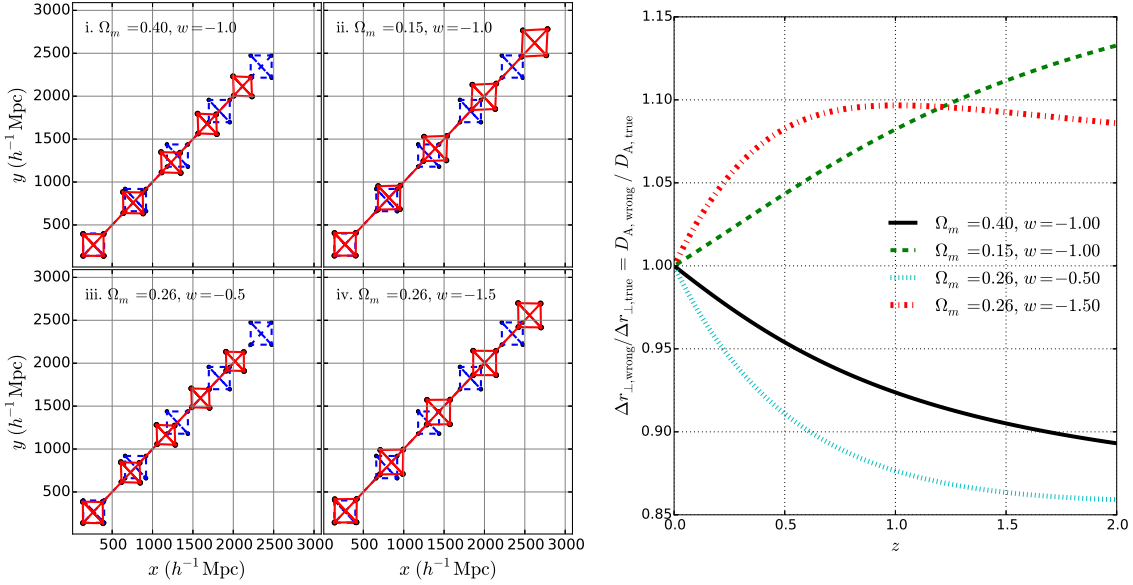


Figure 1. The scaling in four wrongly assumed cosmologies ..., assuming a true cosmology of $\Omega_m = 0.26$, $w = -1$. Left panel shows a series objects distributes as five perfect squares, measured by an observer located at the origin. Their true positions and shapes are plotted in blue dashed lines. The observer measures the redshifts of these objects, adopts the wrong cosmologies to compute the distance, and obtains wrong results (red solid lines). Right panel shows the misestimation of angular diameter distance when the wrong cosmologies are adopted.

The effects due to wrongly assumed cosmological parameters are shown in the upper panel of Figure 1. Suppose that the true cosmology is a flat Λ CDM with present density parameter $\Omega_m = 0.26$ and standard dark energy EoS $w = -1$. If we were to distribute a series of perfect squares at various distances from 500 Mpc/h to 3000 Mpc/h, and an observer located at the origin were to measure their redshifts and compute their positions and shapes using redshift-distance relations of four incorrect cosmologies

- (i). $\Omega_m = 0.40, w = -1.0$,
- (ii). $\Omega_m = 0.15, w = -1.0$,
- (iii). $\Omega_m = 0.26, w = -0.5$,
- (iv). $\Omega_m = 0.26, w = -1.5$,

the shapes of the squares appear distorted (AP effect), and their volumes are changed (volume effect). In the cosmological models in model (i,iii) we see a compression of size (in both angular and LOS direction) and the degree of compression increases with increasing distance, while in models (ii,iv) we see stretch of size whose degree also evolves with redshift. Thus, when wrong cosmological parameters are adopted, the apparent size of objects are distorted, and the magnitude of distortion also varies with redshift.

In this paper we will use the galaxy angular 2pCF to probe the redshift dependence of the distortion in angular direction. In the right panel of Figure 1 we plot the redshift dependence of the change in angular size, $\Delta r_{\perp,\text{wrong}} / \Delta r_{\perp,\text{true}}$, in the four wrong cosmologies. In all cosmologies, there is clear evolution of $\Delta r_{\perp,\text{wrong}} / \Delta r_{\perp,\text{true}}$ in the redshift range $0 < z < 2$. E.g., when use the quintessence cosmology $\Omega_m = 0.26, w = -0.5$ to infer the postions of objects, the angular size is underestimated by 8.9%, 12.3%, 13.6%, 14.1% at $z = 0.5, 1, 1.5, 2$.

3. THE SIMULATION DATA

We test the method on the Horizon Run 4 (HR4) simulation (Kim et al. 2015). HR4 used $N = 6300^3$ particles in a box size of $L = 3150 h^{-1}$ Mpc. It adopted the second order Lagrangian perturbation theory (2LPT) initial conditions at $z_i = 100$ and a WMAP5 cosmology $(\Omega_b, \Omega_m, \Omega_\Lambda, h, \sigma_8, n_s) = (0.044, 0.26, 0.74, 0.72, 0.79, 0.96)$ (Komatsu et al. 2011). The particle mass is $\simeq m_p \simeq 9.02 \times 10^9 h^{-1}$ M $_\odot$.

Mock galaxy samples are produced from the simulation based on a modified one-to-one correspondence scheme (Hong et al. 2016). The most bound member particles (MBPs) of simulated halos are adopted as the tracer of galaxies, and the merger timescale is computed to get the lifetime of merged halos. Merger trees of simulated halos are constructed by tracking their MBPs from $z = 12$ to 0. When a merger event occurs, we adopt the formulae of Jiang et al. (2008) to calculate the merger timescale and determine when a satellite galaxy is completely disrupted.

Hong et al. (2016) compared the 2pCF of the SDSS DR7 volume-limited galaxy sample (Zehavi et al. 2011) and the HR4 $z = 0$ mock galaxies. The mock galaxies shows a similar finger of god (FOG) feature (Jackson 1972) as the observation. On scales greater than $1 h^{-1}$ Mpc, the projected 2pCF of the mock and observational samples agree within 1σ deviation.

The output of HR4 simulation includes one all-sky light cone mock galaxy catalogue reaching $r = 3150 h^{-1}$ Mpc and a series (**how many?**) of snapshot mock galaxy catalogues at different redshifts. In this paper we use five snapshot data at $z = 0, 0.5, 1, 1.5, 2$. We require subhalos to have at least 30 member particles, so the minimal mass of galaxies is $\simeq m_p \simeq 2.7 \times 10^{11} h^{-1}$ M $_\odot$. At the five redshifts, we get a number of 457, 406, 352, 206 and 228 million mock galaxies, corresponding to a number density of 1.46, 1.30, 1.13, 0.98 and 0.73 in unit

of $10^{-2}h^3\text{Mpc}^{-3}$, respectively.

4. GALAXY ANGULAR 2PCF

4.1. Galaxy distribution at different redshifts

The left panels of Figure 2 show the x, y coordinates of galaxies in a $260h^{-1}\text{Mpc} \times 130h^{-1}\text{Mpc} \times 105h^{-1}\text{Mpc}$ volume, taken from the five snapshots. The gravitational growth of structures with decreasing redshift is clearly shown. We display all mock galaxies with $M > 3.0 \times 10^{11}h^{-1}\text{M}_\odot$. At lower redshift, galaxies become more massive, so they are more galaxies satisfying the threshold.

If one adopts a wrong cosmology to compute galaxy positions, there would be a scaling of the galaxy distribution. In the left panel we show the case when a wrong set of parameters $\Omega_m = 0.05, w = -1.5$ is assumed, leading to large upscaling of 25.6%, 47.3%, 62.2%, 71.7% at redshifts $z = 0.5, 1.0, 1.5, 2.5$.

Compared with the true galaxy distribution, the apparent distribution inferred by wrong set of parameters show clear evolution with redshift due to the different scaling at different redshifts. In case of Figure 2, the apparent size of large scale structures increases with redshift.

The growth of structure also make the size of structures evolves with redshift. In the next subsection we will discuss how to distinguish these two effects in the galaxy angular 2pCF.

4.2. Galaxy angular 2pCF: amplitude and shape at different redshifts

The left panel of Figure 3 displays the measured angular 2pCF of galaxies (multiplied by scale r) in the five snapshot.

The amplitude of 2pCF is crucially affected by the cosmic structure growth and the galaxy bias. We find $\xi(z=0) > \xi(z=0.5) > \xi(z=1)$. At low redshift, the large scale structures experienced most gravitational growth, leading to stronger clustering strength and higher amplitude of 2pCF. On the contrary, at higher redshift we find $\xi(z=2) > \xi(z=1.5) > \xi(z=1)$, simply because by applying a uniform mass cut we are selecting more biased galaxies at higher redshift.

Different from the large variation of amplitude among the different redshifts, the shape of 2pCF maintains similar at all redshifts. At all redshifts, we see the $r\xi$ peaks at $r \sim 9h^{-1}\text{Mpc}$, and monotonically drops at larger or smaller scales. The only exception is the relative enhancement of 2pCF at $r \lesssim 2h^{-1}\text{Mpc}$, which is caused by the non-linear growth of structures on small scales and becomes more dramatic at lower redshift.

The middle panel of Figure 3 displays the $r\xi$ normalized by the overall amplitude within $5h^{-1}\text{Mpc} < r < 50h^{-1}\text{Mpc}$ (here after $\hat{r}\xi$). The nice overlapping of the results from five redshifts suggests small evolution of shape with redshift. In the right panel, we compare the high redshift $\hat{r}\xi$ to the $z=0$ result. There is 1-4% relative enhancement at $r < 10h^{-1}\text{Mpc}$, and < 1.5% relative suppression at $r > 25h^{-1}\text{Mpc}$. The trend is monotonic with redshift.

In all, we conclude that the shape of the 2pCF is more robust than the amplitude against redshift and galaxy bias.

4.3. Galaxy angular 2pCF: in wrong cosmologies

When a wrong set of cosmological parameters is adopted, the galaxy distribution is artificially scaled. This scaling is expected to change the shape of the 2pCF, following the relationship,

$$\hat{\xi}_{\text{wrong}}(r) = \hat{\xi}_{\text{true}}(\alpha_\perp r), \quad (4)$$

a simple consequence of the fact that clustering patterns at distance r now appears on a the scale $\alpha_\perp r$. The redshift evolution of α_\perp leads to redshift evolution of shape.

Lower panels of Figure 3 shows the $r\xi$ in five snapshots, in case that the cosmology $\Omega_m = 0.05, w = -1.5$ is adopted to construct the galaxy distribution (the right panels of Figure 2). The middle panel displays the clear redshift evolution of shape of $r\xi$. E.g., from $z=0$ to $z=2$, the peak location is shifted from $r = 9h^{-1}\text{Mpc}$ to $r \sim 15h^{-1}\text{Mpc}$ at $z=2$ since the angular separation is upscaled by 71.7%.

The right panel shows that, at higher redshift, there is a 20-40% change in the value of $r\xi$.

The amplitude of $r\xi$ is amplified due to the stretch of scale. As shown in the left panel, the amplitude monotonically increases as a function of redshift. But this phenomenon can also appear in case of gravitational growth of structure or increasing of bias, so we will not make use of it to do cosmological constraint. We utilize the redshift evolution of the 2pCF shape as a signal suggesting that the assumed cosmological parameters are wrong.

In Figure 5 we further plot the redshift evolution of 2pCF in the four wrong cosmologies of Figure 1. In all cases, the scaling leads to evident redshift evolution of the shape of $r\xi$. When the cosmologies $\Omega_m = 0.4, w = -1$ and $\Omega_m = 0.26, w = -0.5$ are adopted, the compression of structure makes the clustering patterns appears on smaller scales. This leads to “steeper” slope of $r\xi$, and the higher the redshift, the steeper the slope. To the opposite, when adopting the cosmologies $\Omega_m = 0.15, w = -1$ and $\Omega_m = 0.26, w = -1.5$, the stretch of size makes the slope shallower at higher redshifts.

4.4. Systematic effects

4.5. Likelihood Analysis

One can build up a likelihood function to describe how significant is the redshift evolution of the 2pCF shape so that to determine whether the adopted cosmological parameters are correct.

$$\chi^2 \equiv \sum_{i=2}^6 \sum_{j_1=1}^{n_\mu} \sum_{j_2=1}^{n_\mu} \mathbf{p}(z_i, \mu_{j_1}) (\mathbf{Cov}_i^{-1})_{j_1, j_2} \mathbf{p}(z_i, \mu_{j_2}), \quad (5)$$

where $\mathbf{p}(z_i, \mu_j)$ is the redshift evolution of clustering, $\hat{\xi}_{\Delta s}$, with systematic effects subtracted

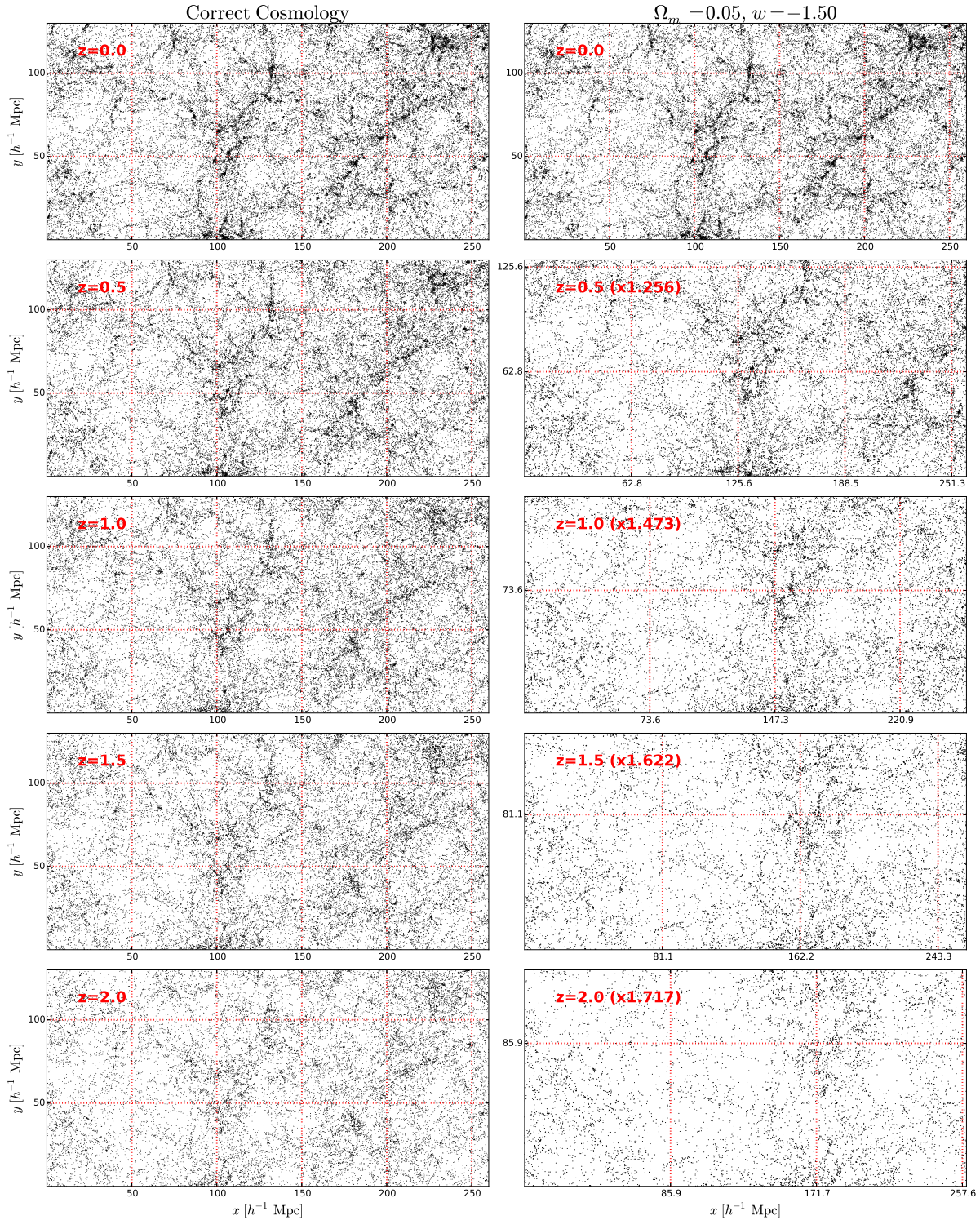
$$\mathbf{p}(z_i, \mu_j) \equiv \delta \hat{r}\xi(z_i, z_1, \mu_j) - \delta \hat{r}\xi_{\text{sys}}(z_i, z_1, \mu_j) \quad (6)$$

\mathbf{Cov}_i is the covariance matrix estimated from the 72 sets of PSB mock galaxies identified from HR3 N-body simulation.

5. COSMOLOGICAL CONSTRAINT

6. METHODOLOGY

We measure the angular 2pCF in the five redshifts. We determine cosmological parameters by examining the redshift evolution of clustering anisotropy. Mock survey samples are used to correct the results for the systematics and to estimate the covariance.

**Figure 2.** blah

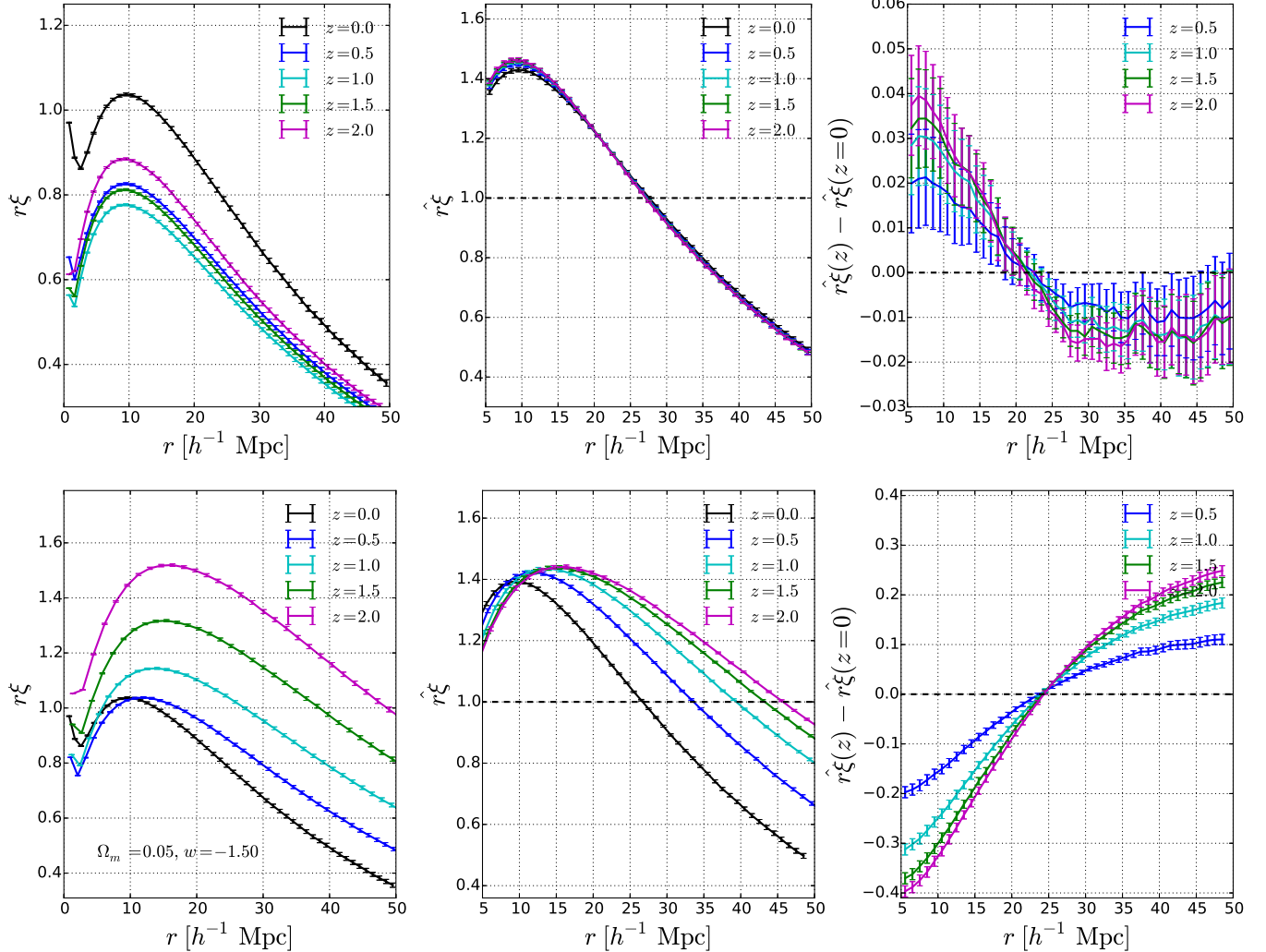
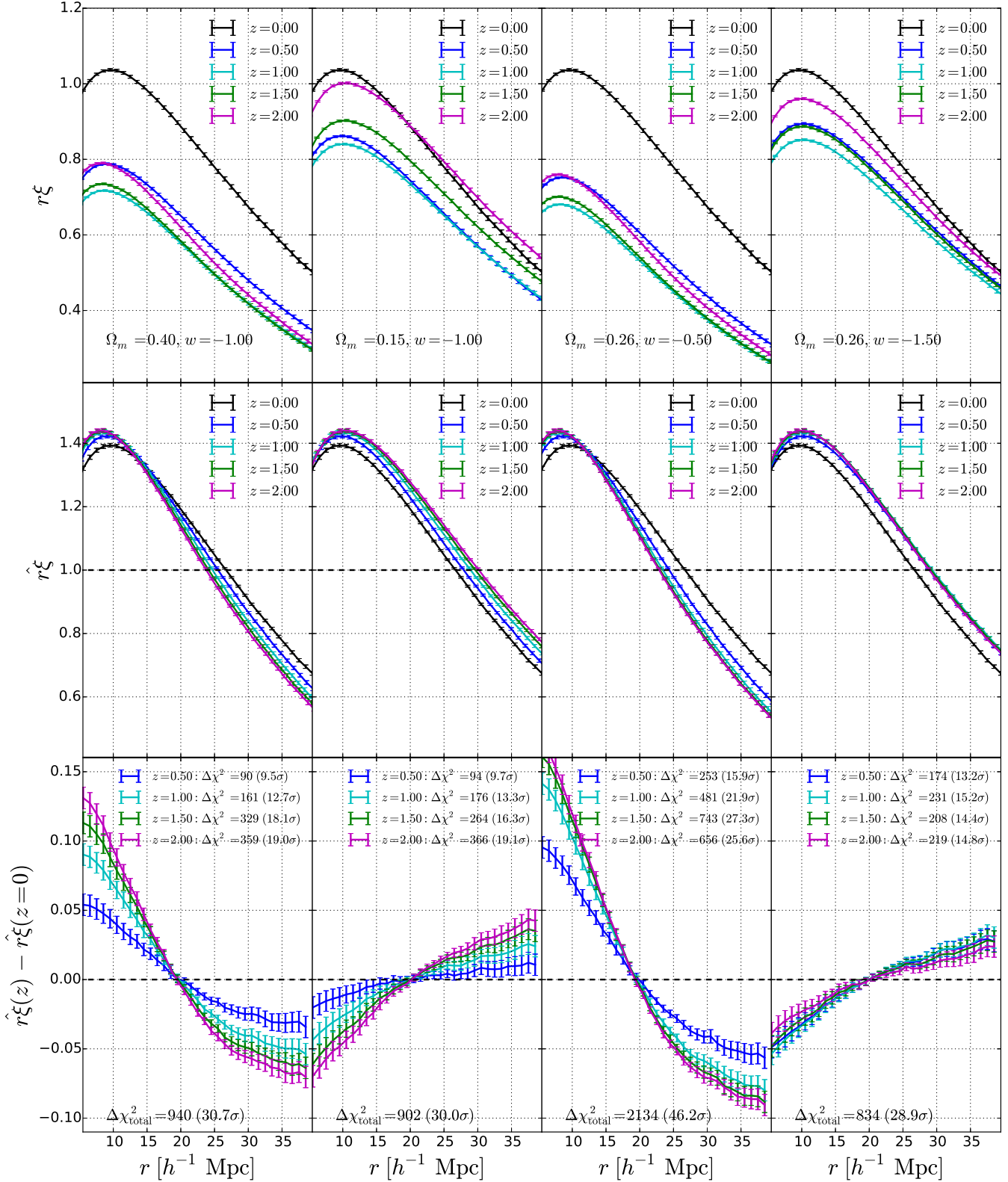


Figure 3. 2pCF at different redshifts.

Figure 4. 2pCF in cosmologies.



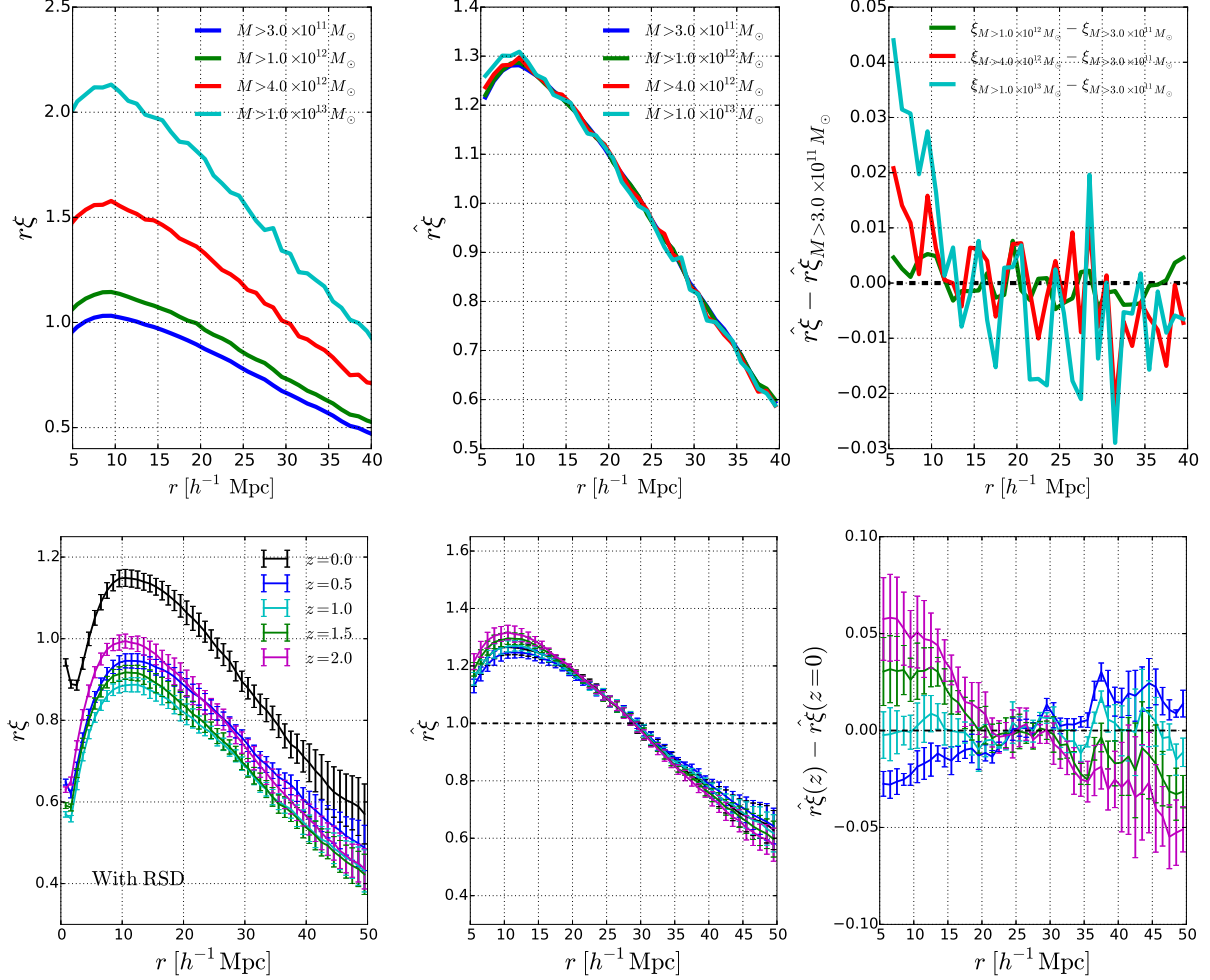


Figure 6. Systematic effects.

6.1. Grid of cosmology parameters

The observed coordinates (RA , Dec , z) of galaxies need to be converted to comoving coordinates (x , y , z) for the 2pCF analysis. The dependence of clustering anisotropy on cosmology enters through the conversion from redshift to comoving distance, i.e. the distance-redshift relation $r(z)$. We consider the case of a flat Universe dominated by matter and dark energy, so our $r(z)$ is governed by two parameters, Ω_m and w , as presented in Equation (2)

To constrain these two parameters we examine the parameter space of $0.06 \leq \Omega_m \leq 0.41$ and $-1.5 \leq w \leq -0.4$ with intervals of $\delta\Omega_m = 0.005$ and $\delta w = 0.025$, forming a 71×45 grid. For each set of (Ω_m, w) , the comoving coordinates of all galaxies are computed, and the 2pCF is ready to be calculated.

6.2. Measuring the correlation function

We adopt the Landy-Szalay estimator (Landy & Szalay 1993) to calculate the 2pCF,

$$\xi(s, \mu) = \frac{DD - 2DR + RR}{RR}, \quad (7)$$

where DD is the number of galaxy–galaxy pairs, DR the number of galaxy-random pairs, and RR is the number of random-random pairs, all separated by a distance defined by $s \pm \Delta s$ and $\mu \pm \Delta\mu$, where s is the distance between the pair and $\mu = \cos(\theta)$, with θ being the angle between the line joining the pair of galaxies and the LOS direction to the target galaxy. This statistic captures the anisotropy of the clustering signal.

The random catalogue consists of unclustered points whose number density in redshift space mimics the radial selection function of the observational data. To reduce the statistical variance of the estimator we use 50 times as many random points as we have galaxies. The galaxies and random points are weighted as described in Sec. 3.

Figure 7 shows the 2D contour of measured ξ as a function of μ and s , from the six redshift bins of LOWZ and CMASS samples in the cosmology of $\Omega_m = 0.31$ Λ CDM model. Due to the peculiar velocity effect, the contour lines are not horizontal. The FOG (Jackson 1972) and Kaiser (Kaiser 1987) effects clearly manifest themselves through the tilting of contour lines in regions of $\mu \rightarrow 1$ and $1 - \mu \gtrsim 0.1$, respectively. A visual inspection of the contour maps from the six redshift bins reveals that they all have a similar appearance, implying small redshift evolution of ξ .

6.3. Probing the anisotropy through 2pCF

The 2pCF is measured as a function of the separation s and the angular direction μ . To probe the anisotropy we are more interested in the dependence of the 2pCF on μ . We follow the procedure of Li et al. (2015) and integrate the ξ over the interval $s_{\max} \leq s \leq s_{\min}$. We evaluate

$$\xi_{\Delta s}(\mu) \equiv \int_{s_{\min}}^{s_{\max}} \xi(s, \mu) ds. \quad (8)$$

The integration is limited at both small and large scales. At small scales the value of ξ is seriously affected by the FOG effect (Jackson 1972) which depends on the galaxies bias. This may introduce a redshift evolution in $\xi_{\Delta s}(\mu)$ that is relatively difficult to model. At large scales the measurement is dominated by noise due to poor statistics. Li et al. (2015) found that $s_{\min} = 6 - 10$

$h^{-1}\text{Mpc}$ and $s_{\max} = 40 - 70 h^{-1}\text{Mpc}$ are reasonable choices which provide consistent, tight and unbiased constraints on cosmological parameters. In this analysis we choose $s_{\min} = 6 h^{-1}\text{Mpc}$ and $s_{\max} = 40 h^{-1}\text{Mpc}$.

The redshift evolution of the bias of observed galaxies leads to redshift evolution of the strength of clustering, which is difficult to accurately model. To mitigate this systematic uncertainty we rely on the shape of $\xi_{\Delta s}(\mu)$, rather than its amplitude,

$$\hat{\xi}_{\Delta s}(\mu) \equiv \frac{\xi_{\Delta s}(\mu)}{\int_0^{\mu_{\max}} \xi_{\Delta s}(\mu) d\mu}. \quad (9)$$

We impose a cut $\mu < \mu_{\max}$ to reduce the fiber collision and FOG effects which are stronger toward the LOS ($\mu \rightarrow 1$) direction.

The clustering properties may be affected by various properties of the galaxy sample, such as, for example the mass, morphology, color, concentration. In our simulation, using the merger tree, we identify “galaxies”, therefore we only use the galaxy mass building history to simulate BOSS galaxies. Therefore, it is necessary for us to test if our mock galaxies can accurately reproduce the $\hat{\xi}_{\Delta s}(\mu)$ of observed galaxies.

Figure ?? compares the shape of $\hat{\xi}_{\Delta s}(\mu)$ measured from observational data and mock survey samples. It is clear that $\hat{\xi}_{\Delta s}(\mu)$ from mock galaxies identified in the HR4 simulation (green dotted line) agrees well with the observation. The enhancement near $\theta = 0^\circ$ is caused by the FOG effect, and the characteristic shape in $20^\circ \lesssim \theta \lesssim 90^\circ$ produced from the large-scale flow are all very well reproduced. This result verifies the ability of our mock galaxies to reproduce the clustering properties of the observed galaxies. The small overestimate (underestimate) of $\hat{\xi}_{\Delta s}$ at large (small) μ could be due to that our mocks galaxies are more massive than those in the observations. We use the HR4 galaxy mocks to correct the systematics.

We divide the full angular range $0 \leq \mu \leq \mu_{\max}$ into n_μ bins and measure its value in each bin. Since we are free to choose μ_{\max} and n_μ , they are varied to optimize the S/N of our results. This topic will be discussed in Sec. ??.

6.4. Characterizing the redshift evolution

As shown in Figure ??, we split the BOSS DR12 galaxies into six redshift bins, three in LOWZ and three in CMASS. To study the redshift evolution of the clustering anisotropy we use the *first redshift bin* as the reference and compare the measurements in other bins with that in the first. We define

$$\delta\hat{\xi}_{\Delta s}(z_i, z_1, \mu_j) \equiv \hat{\xi}_{\Delta s}(z_i, \mu_j) - \hat{\xi}_{\Delta s}(z_1, \mu_j) \quad (10)$$

where $\hat{\xi}_{\Delta s}(z_i, \mu_j)$ is $\hat{\xi}_{\Delta s}$ measured in the i th redshift bin and j th μ bin, where $1 \leq i \leq 6$ and $1 \leq j \leq n_\mu$. To characterize the shape of the curve well $n_\mu \gtrsim 5$ is required.

6.5. Correction for systematics

Other than the AP effect, there are additional effects which may produce redshift-dependent anisotropy and affect the results.

The observational artifacts, such as fiber collisions, redshift failures, and the non-cosmological density fluctuations with stellar density and seeing, are accounted

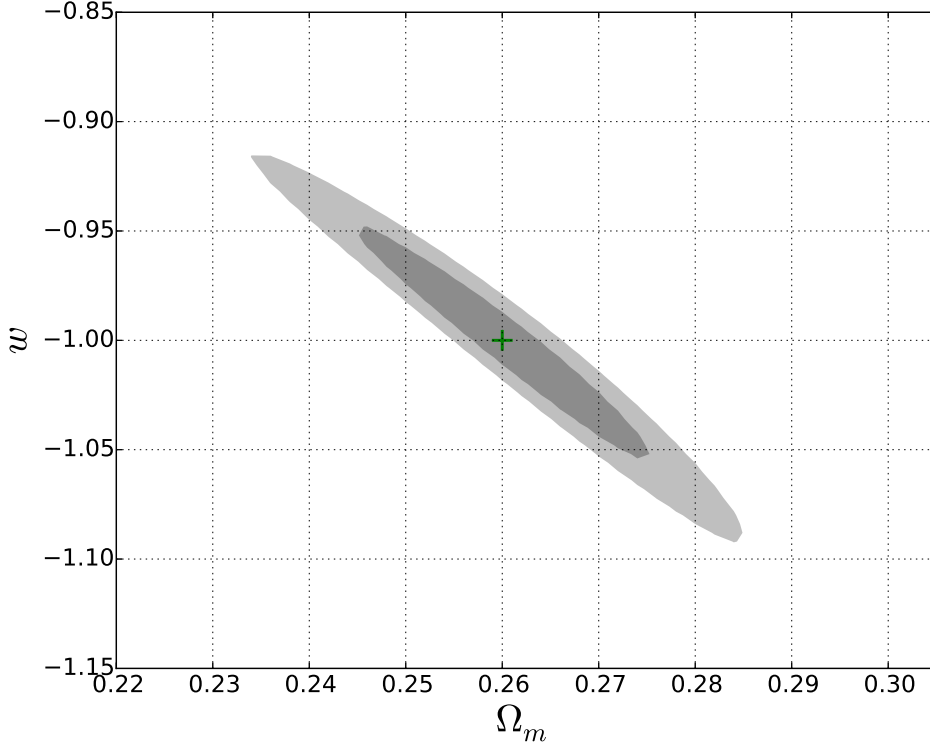


Figure 7. 2D contour map of measured ξ as a function of μ and s , from the six redshift bins of LOWZ and CMASS samples in the cosmology of $\Omega_m = 0.31$ Λ CDM model. The black dashed lines mark the scales $6 h^{-1} \text{Mpc} \leq s \leq 40 h^{-1} \text{Mpc}$. The contour lines are not horizontal due to the effects of peculiar velocity. The FOG and Kaiser effects clearly manifest themselves through the tilting of contour lines where $1 - \mu \rightarrow 0$ and $1 - \mu \gtrsim 0.1$, respectively. The six contour maps have rather similar appearance, implying small redshift evolution of ξ .

for in the galaxy weights (Reid et al. 2016). Fiber collisions and redshift failures may affect the value of $\hat{\xi}(\mu)$ in the region close to LOS; we abandon the angular region of $1 - \mu < 0.01$, to avoid possible systematics (see Appendix ?? for more discussion).

The non-contiguous NGC and SGC are less well cross-calibrated with respect to each other than they are internally calibrated (Schlafly et al. 2010; Schlafly & Finkbeiner 2011; Parejko et al. 2013). We construct the NGC and SGC mock surveys separately to avoid possible systematics. The 2pCF analysis is also carried out for the NGC and SGC independently. The result should be robust as long as each catalogue is well calibrated internally.

The apparent anisotropy introduced by RSD is, although greatly reduced by focusing on the redshift evolution, still the most significant systematic effect.

We estimate the value of $\hat{\xi}_{\Delta s}$ from the systematic effects and subtract their contribution (hereafter $\hat{\xi}_{\Delta s, \text{sys}}$) from the total variation. The quantity $\hat{\xi}_{\Delta s, \text{sys}}$ is estimated from the HR4 mock galaxies. The mock survey sample imitates the SDSS BOSS sample by mimicking the survey as close as possible and includes past light cone effects. The observational systematics such as the RSD, survey geometry, and shot noise are included in the exactly same way as the observation. The peculiar velocity perturbs the observed redshift through the relation

$$\Delta z = (1 + z) \frac{v_{\text{LOS}}}{c}, \quad (11)$$

where v_{LOS} is the LOS component of the peculiar velocity of galaxies. The redshift evolution of galaxy peculiar velocities, resulting from growth of structure, causes the anisotropy produced by RSD to have a small redshift evolution; this is the main source of systematic uncertainty in our results.

We take the HR4 mock galaxy samples and compute $r(z)$ of galaxies in the cosmology under which the simulation is based. In this case there is no AP effect. Thus, the measured $\delta\hat{\xi}_{\Delta s}$ are the redshift evolution purely created by systematics effects. They are adopted as the estimation of $\hat{\xi}_{\Delta s, \text{sys}}$, and the results are illustrated in Figure 6.

For the 1st to 5th redshift bins, $\delta\hat{\xi}_{\Delta s, \text{sys}}(z_i, z_1) \lesssim 0.02$, indicating a small redshift evolution of the RSD effect and properties of galaxies. The only exception is the 6th redshift bin where the values of $\delta\hat{\xi}_{\Delta s, \text{sys}}(z_6, z_1)$ are relatively large. The reason for the large values is that the galaxies in that highest redshift bin are significantly more massive than those at lower redshifts, so the measured high redshift $\hat{\xi}_{\Delta s}(\mu)$ has larger (smaller) values at $\mu \rightarrow 1$ ($\mu \rightarrow 0$) compared with the others (an investigation of the dependence of $\hat{\xi}_{\Delta s}(\mu)$ on galaxy mass is provided in Sec. 6.6).

6.6. The caveats

Li et al. (2014, 2015) found the RSD effect exhibits a small redshift dependence of $\hat{\xi}_{\Delta s}(\mu)$, mainly due to

the structure growth and the selection effect (different galaxy bias at different redshifts). In this analysis we use the mock galaxy sample from HR4 to correct this systematics. The galaxy assignment scheme of Hong et al. (2016) applied to HR4 is very successful in modeling both the large scale Kaiser effect and the small scale FOG effect in nonlinear regions.

There are two possible caveats in our procedure of the modeling of the RSD effect.

1) The RSD effect is estimated from mock survey samples created in a particular cosmology, i.e., the $\Omega_m = 0.26$ Λ CDM model. If this adopted cosmology is different from the truth, then there could be a systematic bias in the estimation. We believe that this will not seriously affect our cosmological constraints. Li et al. (2014) shows that the redshift dependence of RSD is not sensitive to cosmological parameters. Also, the cosmologies adopted in the HR3 and HR4 simulations are consistent with our best-fit cosmological parameters within 1σ , therefore our inferred cosmological constraints should be fairly accurate. In a future analysis, we will estimate the redshift evolution of the RSD effect from a set of cosmological simulations covering the relevant part of the parameter space. This approach will remove the remaining uncertainty associated with the RSD effect, which is already a minor effect in our analysis.

2) The selection effect, i.e., the evolution of galaxy bias with redshifts, can introduce redshift evolution in the clustering properties of the observed galaxies. In our analysis the amplitude of the 2pCF is normalized and only its angular information, the function $\hat{\xi}_{\Delta s}(\mu)$, is used. This function is rather insensitive to the galaxy bias, which mainly affects the strength of clustering.

As a test, Figure ?? shows $\hat{\xi}_{\Delta s}(\mu)$ measured from a small HR4 galaxy sample with different minimal mass cuts. The mock galaxies are taken from the $z = 0$ snapshot data within the radius $r < 600 h^{-1}$ Mpc. Applying the minimal mass cuts of $1, 2, 4 \times 10^{13} h^{-1} M_\odot$, we created three sets of subsamples with number density of $n = 4.56, 2.10, 0.91 \times 10^{-4} (h^{-1} \text{Mpc})^{-3}$, which roughly covers the scatter of the number density of BOSS DR12 galaxies at $0.15 < z < 0.7$ ².

For subsamples with higher mass cuts the $\hat{\xi}_{\Delta s}(\mu)$ has larger (smaller) values at $\mu \rightarrow 1$ ($\mu \rightarrow 0$). More massive samples result in less tilted $\hat{\xi}_{\Delta s}(\mu)$ in the region of $1 - \mu \gtrsim 0.1$ ³. This explains the relative large value of $\hat{\xi}_{\Delta s, \text{sys}}(z_6, z_1)$. In particular, comparing the subsamples with mass cuts $4 \times 10^{13} h^{-1} M_\odot$ and $1 \times 10^{13} h^{-1} M_\odot$, we find the red dotted curve is higher (lower) than the blue solid line at $\mu \rightarrow 1$ ($\mu \rightarrow 0$), with a difference of ≈ 0.1 (0.05), consistent with the value of $\hat{\xi}_{\Delta s, \text{sys}}(z_6, z_1)$ shown

² The BOSS LOWZ and CMASS galaxies reside in massive haloes with a mean halo mass of $5.2 \times 10^{13} h^{-1} M_\odot$ and $2.6 \times 10^{13} h^{-1} M_\odot$ (Parejko et al. 2013; White 2011; Reid et al. 2016), respectively. For CMASS galaxies, when the redshift changes from $z = 0.43$ to 0.7 , the mean stellar mass varies from $10^{11.6} M_\odot$ to $10^{11.9} M_\odot$ (Parikh et al. 2014).

³ This phenomenon is understandable. The tilt of $\hat{\xi}_{\Delta s}(\mu)$ is related to the RSD effect, and also the overall amplitude of the 2pCF (the denominator of Eq. (9)). The slope should be roughly proportional to $(v/b_g)^2$, where the peculiar velocity term v^2 denotes the effect of RSD, and the galaxy bias term b_g^2 represents the amplitude of the 2pCF. For the more massive sample, b_g is much larger while v is still close to the peculiar velocity of dark matter field, therefore the slope is smaller.

in Figure 6.

In addition, this result also explains the small discrepancy between the $\hat{\xi}_{\Delta s}(\mu)$ measured from the observational data and the HR4 simulations (Figure ??). The mock galaxies could be systematically more massive than the observed ones. These systematics could be most significant in the 6th redshift bin where mock galaxies are most massive, leading to possible overestimation of $\delta\hat{\xi}_{\Delta s, \text{sys}}$. We discuss the impact of this effect in Sec. 6.1.

Considering the large variation of mass cuts, the change of $\hat{\xi}_{\Delta s}(\mu)$ is not significant, so we conclude that $\hat{\xi}_{\Delta s}(\mu)$ is relatively insensitive to the galaxy bias.

6.7. χ^2 function

We define a χ^2 function to quantify the redshift evolution of clustering anisotropy

$$\chi^2 \equiv \sum_{i=2}^6 \sum_{j_1=1}^{n_\mu} \sum_{j_2=1}^{n_\mu} \mathbf{p}(z_i, \mu_{j_1}) (\mathbf{Cov}_i^{-1})_{j_1, j_2} \mathbf{p}(z_i, \mu_{j_2}), \quad (12)$$

where $\mathbf{p}(z_i, \mu_j)$ is the redshift evolution of clustering, $\hat{\xi}_{\Delta s}$, with systematic effects subtracted

$$\mathbf{p}(z_i, \mu_j) \equiv \hat{\xi}_{\Delta s}(z_i, z_1, \mu_j) - \hat{\xi}_{\Delta s, \text{sys}}(z_i, z_1, \mu_j) \quad (13)$$

\mathbf{Cov}_i is the covariance matrix estimated from the 72 sets of PSB mock galaxies identified from HR3 N-body simulation.

6.8. Cosmological Constraints

We constrain Ω_m and w through Bayesian analysis (Christensen et al. 2001), which derives the probability distribution function (PDF) of some parameters θ ($= (\Omega_m, w)$ in this paper) given observational data \mathbf{D} , according to Bayes' theorem:

$$P(\theta|\mathbf{D}) = \frac{P(\theta)P(\mathbf{D}|\theta)}{m(\mathbf{D})}. \quad (14)$$

Here $P(\theta)$, the prior distribution of the parameters, contains all the information about the parameters known from substantive knowledge and expert opinion *before* observing the data. The marginal PDF of \mathbf{D} , $m(\mathbf{D}) = \int P(\mathbf{D}|\theta)P(\theta)d\theta$, is a normalization constant independent of θ . All the information about the parameter θ that stems from the experiment is contained in the function $P(\mathbf{D}|\theta)$, the conditional PDF of the observation \mathbf{D} given the value of parameter.

In this analysis we simply assume flat priors for Ω_m and w , and approximate $P(\mathbf{D}|\theta)$ by a likelihood function \mathcal{L} satisfying $-2 \ln \mathcal{L} = \chi^2$; the PDF of θ derived from our AP method takes the form

$$P(\theta|\mathbf{D}) \propto \mathcal{L} \propto \exp \left[-\frac{\chi^2}{2} \right]. \quad (15)$$

We use the COSMOMC software (Lewis & Bridle 2002) to obtain the Markov Chain Monte Carlo (MCMC) samples of θ following the PDF of $P(\theta|\mathbf{D})$. Constraints on Ω_m and w are derived from these samples.

The 68% and 95% likelihood contours of Ω_m and w obtained from this analysis are shown in Figure ?? (pink areas). Our AP method yields tight constraints on Ω_m and w . The mean values and 68% CL are

$$\Omega_m = 0.314 \pm 0.038, \quad w = -1.09 \pm 0.14. \quad (16)$$

Figure 8. Likelihood contours (68.3%, 95.4%) in the $\Omega_m - w$ plane from our method.

This result is consistent with the Planck Λ CDM cosmology within 1σ (Ade et al. 2015).

7. CONCLUDING REMARKS

- * Can be combined with our redshift dependence of AP to full explore the geometric effects in LSS
- * *** utilizes angular 2pCF as a function of redshift. Our method is complementary to it: 1) smaller scales; 2) more bins; 3) could be less affected by RSD; ... In case of good modelling of RSD one can rely on their; in case not possible, especially on small scales, one can use ours

- * Complementary to all other LSS probes
- * Promising future

ACKNOWLEDGMENTS

We thank the Korea Institute for Advanced Study for providing computing resources (KIAS Center for Advanced Computation Linux Cluster System). We would like to thank Yi Zheng for useful discussions. This work was partially supported by the Supercomputing Center/Korea Institute of Science and Technology Information with supercomputing resources including technical support (KSC-2013-G2-003).

APPENDIX

REFERENCES

- Ade, P.A.R., Aghanim, N., & Arnaud, M., et al. arXiv:1502.01589
 Alam, S., Ata, M., & Bailey, S., et al. 2016, submitted to MNRAS (arXiv:1607.03155)
 Alam S., Albareti, F.D., & Allende Prieto, C., et al., 2015, ApJS, 219, 12
 Alcock, C., & Paczynski, B. 1979, Nature, 281, 358
 Anderson, L., Aubourg, É., & Bailey, S. et al. 2014, MNRAS, 441, 24
 Ballinger, W.E., Peacock, J.A., & Heavens, A.F. 1996, MNRAS, 282, 877
 Betoule, M., Kessler, R., & Guy, J., et al. 2014, A&A, 568, 32
 Beutler, F., Blake, C., & Colless, M., et al. 2011, MNRAS, 416, 3017
 Beutler, F., Saito, S., & Seo, H.-J., et al. 2013, MNRAS, 443, 1065
 Beutler, F., Seo, H.-J., & Saito, S., et al. 2016, arXiv:1607.03150
 Blake, C., Glazebrook, K., & Davis, T. M., 2011, MNRAS, 418, 1725
 Blake, C., James, J.B., & Poole, G.B. 2013, MNRAS, 437, 2488
 Bolton, A.S., Schlegel, & D.J., Aubourg E., et al. 2012, AJ, 144, 144
 Boylan-Kolchin, M., Ma, C.-P., & Quataert, E. 2008, MNRAS, 383, 93
 Christensen, N., Meyer, R., Knox, L., & Luey, B. 2001, Class. Quant. Grav., 18, 2677
 Chuang, C.-H., & Wang, Y. 2012, MNRAS, 426, 226
 Dawson, K.S., Kneib, J.P., & Percival, W.J., et al. 2015, accepted AJ
 Dawson, K.S., Schlegel, D.J., & Ahn, C.P., et al. 2012, AJ, 145, 10
 Efstathiou, G. 2014, MNRAS, 440, 1138
 Eisenstein, D.J., Weinberg, D.H., & Agolet, E., et al. 2011, AJ, 142, 72
 Feldman, H.A., Kaiser, N., & Peacock, J.A. 1994, ApJ, 426, 23
 Fukugita, M., Ichikawa, T., & Gunn, J.E., et al. 1996, AJ, 111, 1748
 Gunn, J.E., Carr, M., & Rockosi, C. et al. 1998, AJ, 116, 3040
 Gunn, J.E., Siegmund, W.A., & Mannery, E.J., et al. 2006, AJ, 131, 2332
 Guzzo, L., Pierleoni, M., & Meneux, B., et al. 2008, Nature, 451, 541
 Hartlap J., Simon P. & Schneider P. [astro-ph/0608064].
 Hong, S.E., Park, C., & Kim, J. 2016, ApJ, 823, 103
 Jackson, J. 1972, MNRAS, 156, 1
 Jennings, E., Baugh, C.M., & Pascoli, S. 2011, MNRAS, 420, 1079
 Jiang, C.Y., Jing, Y. P., & Faltenbacher, A., et al. 2008, ApJ, 675, 1095
 Kaiser, N. 1987, MNRAS, 227, 1
 Kim, J., & Park, C. 2006, ApJ, 639, 600
 Kim, J., Park, C., Gott, J.R., III, & Dubinski, J. 2009, ApJ, 701, 1547
 Kim, J., Park, C., L'Huillier, B., & Hong, S. E. 2015, JKAS, 48, 213
 Kim, J., Park, C., Rossi, G., Lee, S.M., & Gott, J.R. 2011, JKAS, 44, 217
 Kitaura, F.S., Rodríguez-Torres, S., Chuang, C.-H., et al. arXiv:1509.06400
 Komatsu, E., Smith, K. M., & Dunkley, J., et al. 2011, ApJS, 192, 18
 Lacey, C., & Cole, S. 1993, MNRAS, 262, 627
 Landy, S.D., & Szalay, A.S. 1993, ApJ, 412, 64
 Laureijs, R., Amiaux, J., & Arduini, S., et al. 2011, arXiv:1110.3193
 Lavaux, G., & Wandelt, B.D. 2012, ApJ, 754, 109
 Lewis, A., & Bridle, S. 2002, Phys. Rev. D, 66, 103511
 L'Huillier, B., Park, C., & Kim, J. 2014, New Astronomy, 30, 79
 Li, M., Li, X.-D., Wang, S., & Wang, Y. 2011, Commun. Theor. Phys., 56, 525
 Li, X.-D., Park, C., Forero-Romero, J., & Kim, J. 2014, ApJ, 796, 137
 Li, X.-D., Park, C., Sabiu, C.G., & Kim, J. 2015, MNRAS, 450, 807
 Li, X.-D., Park, C., Sabiu, C.G., & Kim, J. 2016, submitted to ApJ
 Linder, E.V., Minji, O., Okumura, T., Sabiu, C.G., & Song, Y.-S. 2014, Phys. Rev. D, 89, 063525
 López-Corredoira, M. 2014, ApJ, 781, 96
 Marinoni, C., & Buzzi, A. 2010, Nature, 468, 539
 Matsubara T., & Suto, Y. 1996, ApJ, 470, L1
 McCavana, T., Micic, M., Lewis, G. F., et al. 2012, MNRAS, 424, 361
 Morandi, A., & Sun, M. arXiv:1601.03741
 Outram, P.J., Shanks, T., Boyle, B.J., Croom, S.M., Hoyle, F., Loaring, N.S., Miller, L., & Smith, R.J. 2004, MNRAS, 348, 745
 Parejko J.K., et al., 2013, MNRAS, 429, 98
 Parihar, P., Vogeley, M.S., & Gott, J.R., et al. 2014, ApJ, 796, 86
 Park, C., Kim, J., & Gott, J.R. 2005, ApJ, 633, 1
 Park, C., & Kim, Y.-R. 2010, ApJL, 715, L185
 Park, C., Choi, Y.-Y., Kim, J., Gott, J.R., Kim, S.S., & Kim, K.-S. 2012, ApJ, 759, 7
 Park, C., Song, H., Einasto, M., Lietzen, H., & Heinamaki, P. 2015, JKAS, 48, 75
 Peebles, P.J.E., & Ratra, B. 2003, Reviews of Modern Physics, 75, 559
 Percival, W.J., Ross, A.J., & Sánchez, A.G., et al. 2014, MNRAS, 439, 2531
 Perlmutter, S., Aldering, G., & Goldhaber, G., et al. 1999, ApJ, 517, 565
 Press, W.H., & Schechter, P.L. 1974, ApJ, 187, 425
 Reid, B., Samushia, L., & White, M., et al. 2012, MNRAS, 426, 2719
 Reid, B., Ho, S., & Padmanabhan, N., et al. 2016, MNRAS, 455, 1553
 Riess, A.G., Filippenko, A.V., & Challis, P., et al. 1998, AJ, 116, 1009
 Riess, A.G., Macri, L., & Casertano, S., et al. 2011, ApJ, 730, 119
 Ross, A.J., Percival, W.J., & Sánchez, A.G. et al. 2012, MNRAS, 424, 564
 Ross, A.J., Samushia, L., & Howlett, C., et al. 2015, MNRAS, 449, 835
 Ryden, B.S. 1995, ApJ, 452, 25
 Sanchez, A. G., Scoccimarro, R., & Crocce, M., et al. arXiv:1607.03147

- Schlafly E.F., Finkbeiner D.P., Schlegel D.J., et al. 2010, ApJ, 725, 1175
- Schlafly E.F., & Finkbeiner D.P. 2011, ApJ, 737, 103
- Schlegel, D., Abdalla, F., & Abraham, T., et al. 2011, arXiv:1106.1706
- Smee, S.A., Gunn, J.E., & Uomoto, A., et al. 2013, AJ, 146, 32
- Song, Y.S., Sabiu, C.G., Okumura, T., Oh, M., & Linder, E.V. 2014, JCAP, 12, 005
- Speare, R., Gott, J.R., Kim, J., & Park, C. 2015, ApJ, 799, 176
- Viana, P.T.P., & Liddle, A.R. 1996, MNRAS, 281, 323
- Villalobos, Á., De Lucia, G., Weinmann, S.M., Borgani, S., & Murante, G. 2013, MNRAS, 433, L49
- Weinberg, S. 1989, Reviews of Modern Physics, 61, 1
- White M., et al. 2011, ApJ, 728, 126
- York, D.G., Adelman, J., & Anderson, J.E., et al. 2000, AJ, 120, 1579
- Zehavi, I., Zheng, Z., & Weinberg, D.H., et al. 2011, ApJ, 736, 59